JGR Space Physics

RESEARCH ARTICLE
10.1029/2022JA031148

Reducing the Ionospheric Contamination Effects on the Column O/N_2 Ratio and Its Application to the Identification of Non-Migrating Tides

Christopher S. Krier[1], Scott L. England[1], R. R. Meier[2,3], and Harald U. Frey[4]

[1]Aerospace and Ocean Engineering, Virginia Polytechnic Institute and State University, Blacksburg, VA, USA, [2]Department of Physics and Astronomy, George Mason University, Fairfax, VA, USA, [3]Naval Research Laboratory, Emeritus, Washington, DC, USA, [4]Space Sciences Laboratory, University of California Berkeley, Berkeley, CA, USA

Key Points:

- The ionospheric contribution to daytime emissions at 135.6 nm observed by Ionospheric Connection Explorer (ICON) Far-Ultraviolet Imager (ICON-FUV) is estimated using either Global Ionospheric Specification (GIS), International Reference Ionosphere, or ICON Extreme Ultraviolet spectrograph (ICON-EUV) data
- To characterize non-migrating tides in column O/N_2, we generate modified datasets in which ionospheric contamination effects are reduced
- Contrary to the unmodified data set, the modified data set generated using GIS data indicates the DE2 tide during March–April 2020

Supporting Information:

Supporting Information may be found in the online version of this article.

Correspondence to:

C. S. Krier,
ckrier@vt.edu

Citation:

Krier, C. S., England, S. L., Meier, R. R., & Frey, H. U. (2023). Reducing the ionospheric contamination effects on the column O/N_2 ratio and its application to the identification of non-migrating tides. *Journal of Geophysical Research: Space Physics*, *128*, e2022JA031148. https://doi.org/10.1029/2022JA031148

Received 14 NOV 2022
Accepted 9 MAR 2023

Abstract Prior investigations have attempted to characterize the longitudinal variability of the column number density ratio of atomic oxygen to molecular nitrogen ($\Sigma O/N_2$) in the context of non-migrating tides. The retrieval of thermospheric $\Sigma O/N_2$ from far ultra-violet (FUV) emissions assumes production is due to photoelectron impact excitation on O and N_2. Consequently, efforts to characterize the tidal variability in $\Sigma O/N_2$ have been limited by ionospheric contamination from $O^+ + e$ radiative recombination at afternoon local times (LT) around the equatorial ionization anomaly. The retrieval of $\Sigma O/N_2$ from FUV observations by the Ionospheric Connection Explorer (ICON) provides an opportunity to address this limitation. In this work, we derive modified $\Sigma O/N_2$ datasets to delineate the response of thermospheric composition to non-migrating tides as a function of LT in the absence of ionospheric contamination. We assess estimates of the ionospheric contribution to 135.6 nm emission intensities based on either Global Ionospheric Specification (GIS) electron density, International Reference Ionosphere (IRI) model output, or observations from the Extreme Ultra-Violet imager (EUV) onboard ICON during March and September equinox conditions in 2020. Our approach accounts for any biases between the ionospheric and airglow datasets. We found that the ICON-FUV data set, corrected for ionospheric contamination based on GIS, uncovered a previously obscured diurnal eastward wavenumber 2 tide in a longitudinal wavenumber 3 pattern at March equinox in 2020. This finding demonstrates not only the necessity of correcting for ionospheric contamination of the FUV signals but also the utility of using GIS for the correction.

1. Introduction

The propagation and dissipation of large-scale atmospheric waves play an important role in the dynamics of the thermosphere. Solar thermal atmospheric tides are planetary-scale waves (primarily driven by the absorption of solar radiation) with periods that are subharmonics of a solar day. Non-migrating tides do not follow the apparent motion of the Sun across the sky and some of the most important tidal components have been shown to originate from the lower atmosphere via large-scale tropospheric latent heat release and the differences in absorption of solar radiation caused by the land-sea distribution (Forbes et al., 2006; Hagan & Forbes, 2002). The longitudinal/local time modulation of the mesosphere/lower thermosphere (MLT) winds (Lieberman et al., 2013), neutral temperature (Forbes et al., 2008), and the composition of minor constituents (Oberheide et al., 2013) have been observed to correlate with the signatures of non-migrating tides. Additionally, the tidal impact on the ionosphere has been well documented in observations (Immel et al., 2006; Sagawa et al., 2005) and has been confirmed by model simulations (Chang et al., 2013; Goncharenko et al., 2010; Pedatella et al., 2011).

The tidal nomenclature used in this paper is standard in the literature. DE3, for example, is the diurnal tide (24 hr period) that is eastward propagating with zonal wavenumber 3 at a fixed universal time. Likewise, SW1 is the semidiurnal tide (12 hr period) that is westward propagating with zonal wavenumber 1 at a fixed universal time. A tide with period, in cycles per day, n and zonal wavenumber s (where $s < 0$ indicates eastward propagation) causes a longitudinal wavenumber $|n - s|$ in a reference frame relative to a fixed local solar time (Forbes et al., 2008).

The column number density ratio of atomic oxygen to molecular nitrogen, referred to as $\Sigma O/N_2$, is a diagnostic of the relative variability of thermospheric composition first proposed by Strickland et al. (1995) and Evans et al. (1995) as a means of retrieving atmospheric composition information from measurements of the ratio of photoelectron-excited OI

135.6 nm/N_2 LBH bands in the far ultra-violet (FUV). It has been hypothesized that non-migrating tides substantially impact the $\Sigma O/N_2$ ratio. Atmospheric theory predicts that tides perturb $\Sigma O/N_2$ as a result of the species-dependent impact of the vertical tidal winds (Cui et al., 2014; England et al., 2021). Indeed, these fluctuations appear in physics-based models of the thermosphere (England et al., 2010; Jones et al., 2014; Roble & Shepherd, 1997). Variations in $\Sigma O/N_2$ can also modify the photochemical equilibrium of the thermosphere and thus the associated F-region ionospheric density (England, 2012; Lean et al., 2011). Model results suggest that $\Sigma O/N_2$ variations contribute at least ~30% of the total variation in ionospheric density (England et al., 2010). To obtain a complete picture of tidal-ionosphere coupling, it is important that the tidal modification of $\Sigma O/N_2$ be well-understood.

Previous attempts to characterize the tidal perturbations in $\Sigma O/N_2$ focused on retrievals from FUV emissions observed by the Global Ultraviolet Imager (GUVI) onboard the Thermosphere, Ionosphere, Mesosphere Energetics and Dynamics (TIMED) satellite which provided limb observations of $\Sigma O/N_2$ from 2002 to 2007 and on the disk from 2002–present (Christensen et al., 2003; Meier et al., 2015). Zhang et al. (2010) found wave-4 and wave-3 perturbations on the order of 10% of the background GUVI $\Sigma O/N_2$ during the boreal fall and summer seasons respectively, hypothesizing that these can be explained by the influence of the DE3 and DE2 non-migrating tides. Model simulations of England et al. (2010) indicate that a 10% perturbation of $\Sigma O/N_2$, translates to about a one third contribution to the connected ionospheric F-region density variations. A comprehensive analysis of the wavenumber structure found in GUVI $\Sigma O/N_2$ was presented by He et al. (2010). Based on GUVI data from 2002 to 2007, they confirmed that the seasonal variation of the wavenumber-4 structure is consistent with that of the strength of the DE3 tide, but the evolution as a function of local time was found to be stationary instead of eastward as would be expected by modulation caused by DE3.

In addition to those produced by the excitation of the ground state atomic oxygen by the impact of photoelectrons and subsequent deexcitation, OI 135.6 nm emissions can also be produced by $O^+ + e$ radiative recombination (RR) in the F-region of the ionosphere (Meier, 1991). Consequently $\Sigma O/N_2$ retrievals from the thermospheric dayglow can be compromised because large O^+ densities can occur at afternoon local solar times around the equatorial ionization anomaly. Work has been done to demonstrate the impact of the ionospheric contamination on the identification of tides in $\Sigma O/N_2$. With GUVI limb radiance profiles, Kil and Paxton (2011) showed that the longitudinal variations in GUVI $\Sigma O/N_2$ are mainly a consequence of the ionospheric contamination. Kil et al. (2013) subsequently quantified the impact of the ionosphere on the GUVI $\Sigma O/N_2$, estimating the contribution to be about 10%. Correira et al. (2021) estimated a 1%–2% error in $\Sigma O/N_2$ from radiative recombination during periods of low solar and geomagnetic activity. During geomagnetically active periods, the radiative recombination source can potentially result in an error 20% or larger (Lee et al., 2013). Recently, Zhang et al. (2021) presented a new algorithm that separates the thermospheric and ionospheric contributions to the GUVI radiances at 135.6 nm and they show results of clean $\Sigma O/N_2$ that are consistent with $\Sigma O/N_2$ as a purely thermospheric quantity. The approach proposed by Zhang et al. (2021) takes advantage of the emission at 130.4 nm observed by GUVI. Using $\Sigma O/N_2$ from the Global-Scale Observations of the Limb and Disk (GOLD), Krier et al. (2021) showed observations of non-migrating diurnal tides in GOLD $\Sigma O/N_2$ based on dusk—dawn differences and included a discussion of potential ionospheric contamination effect, concluding that the impact could vary by season with the higher impact during boreal fall than that during boreal winter.

Observations of the $\Sigma O/N_2$ ratio from the Far Ultra-violet Imager (FUV) onboard the Ionospheric Connection Explorer (ICON; Immel et al., 2018) provide an opportunity to study non-migrating tides in thermospheric composition (England et al., 2021). Launched in October 2019 into a low Earth orbit, NASA lost contact with ICON in November 2022. The rapid local time precession afforded by the ICON observatory in a 27° inclined orbit is a distinct advantage because seasonal variations do not strongly alias into the tidal signal during the time required to sample all local solar times (~27 days). As indicated by the previous investigations discussed above, the effects of ionospheric contamination must be considered in any tidal analysis of $\Sigma O/N_2$. Since ICON-FUV does not observe emissions at 130.4 nm, the approach proposed by Zhang et al. (2021) is not feasible for ICON. As an alternative approach, we calculate the ionospheric contribution based on a variety of datasets including Global Ionospheric Specification (GIS), the International Reference Ionosphere, and the Extreme Ultraviolet (EUV) instrument on ICON.

The objectives of this study are the following:

1. Calculate the ionospheric contribution to the ICON-FUV observations at 135.6 nm along the line of sight of $\Sigma O/N_2$ retrieval based on three different data sources: GIS, the International Reference Ionosphere (IRI), and the ICON EUV Imager. To scale the calculations such that biases of the datasets are minimized, we leverage nighttime ICON-FUV observations in which only the ionospheric contribution is present.

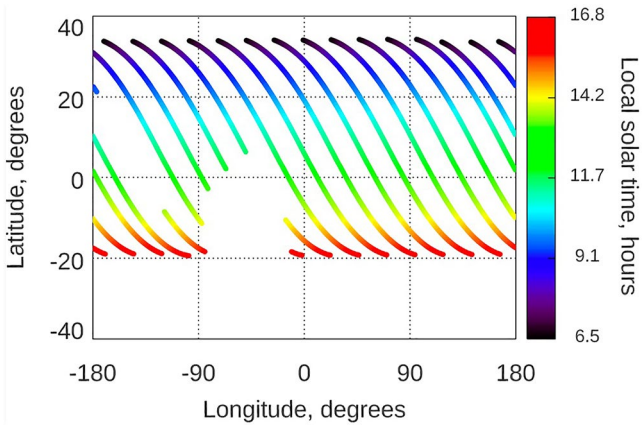

Figure 1. Global distribution and local time sampling of column disk O/N_2 observations on 22 August 2020 from the Far-Ultraviolet imager onboard the Ionospheric Connection Explorer. The gap in the southern hemisphere is due to the South Atlantic Anomaly. The gap between about (20°N, 180°W) and (10°S, 120°W) in one orbit is due to a spacecraft maneuver.

2. Derive modified ICON-FUV $\Sigma O/N_2$ datasets which have been corrected for ionospheric contamination.
3. Delineate the response of $\Sigma O/N_2$ to non-migrating tides as a function of local time and compare amplitudes to those of modeled tides from the Thermosphere Ionosphere Electrodynamics General Circulation Model (TIEGCM). Importantly, identify any changes in the non-migrating tidal structure seen in the original and modified datasets.

This paper is organized as follows. Section 2 describes the data and models used in the present work. Section 3 presents our methodology. Section 4 shows the relevance of the analyses to the three objectives. Section 5 puts Section 4 into context using physics based models. Section 6 contains a summary and closing remarks.

2. Data and Models

2.1. ICON Far-Ultraviolet Observations

The ICON Far-Ultraviolet Imager (ICON-FUV) is a spectrographic imager that observes airglow emissions in two separate wavelength pass-bands: short wave (SW) centered on the OI doublet at 135.6 nm and long wave (LW) including a portion of the Lyman-Birge-Hopfield (LBH) bands centered on 157 nm (Mende et al., 2017). Images of the airglow capture both the Earth's limb up to about 500 km tangent altitude and downward onto the disk to an angle about 58° from nadir. ICON-FUV points perpendicular to the spacecraft velocity vector such that during normal observational conditions, ICON-FUV points true north at the transition between ascending and descending orbit nodes. The thermospheric $\Sigma O/N_2$ is inferred from the ratio of the daytime column brightness intensity ratio of SW to LW on the disk of the Earth about 7.5° angular distance from the ICON observatory (Meier, 2021; Stephan et al., 2018). During conditions of atmospheric darkness, ICON-FUV observes the $O^+ + e$ radiative recombination emission in the SW channel from which O^+ density profiles are derived (Kamalabadi et al., 2018). Wautelet et al. (2021) compared the retrieved nighttime O^+ density profiles to ground-based and COSMIC-2 data sets and found ∼50% positive bias in the ICON-FUV values based on calibrated radiances in Version 3 of the FUV database.

Each image of calibrated column brightness is separated into six vertical stripes each constituting a profile integrating 3° of horizontal field of view. The $\Sigma O/N_2$ disk inversion takes as input the average of 21 pixels on the disk in the stripe corresponding to 0°–3° along the horizontal field of view (referred to as stripe P0 in ICON-FUV Level 1 data products, https://icon.ssl.berkeley.edu/Data/Data-Product-Matrix).

This work uses Version 4 of $\Sigma O/N_2$ data and Version 3 of the calibrated far-ultraviolet radiances, which were the latest available when this work was undertaken. In addition, this work reassesses part of the analysis of England et al. (2021) with the same $\Sigma O/N_2$ data version used therein. Because the focus of this paper is a method to remove the ionospheric contribution from the retrieval of $\Sigma O/N_2$ and its implications for the identification of upward propagating non-migrating tides, the actual version of radiances used is not of primary relevance; data version is accounted for with our calibration method (Section 3). Indeed, the recently released ICON-FUV Version 5 calibrated radiances report generally lower values, which turns out to be supported by this work (see Figure 3 and discussion in Section 3).

ICON flies in a 27° inclined orbit at about 590 km altitude. Figure 1 depicts the global distribution and local solar time sampling of 1 day of ICON-FUV $\Sigma O/N_2$ retrievals on 22 August 2020. The local solar time at any latitude is approximately fixed on any day and quickly moves to early local solar times as a function of day. The large gap in the southern hemisphere is due to the South Atlantic Anomaly where ICON-FUV is turned off. Therefore, we focus analysis on the northern hemisphere where full longitudinal sampling is afforded.

2.2. Global Ionospheric Specification

GIS employs a data assimilative approach to produce hourly three-dimensional global maps of electron density (Lin et al., 2017; Lin, Lin, Liu, 2020). Radio occultations from COSMIC-2 and ground-based observations of

slant Total Electron Content (TEC) are assimilated into the nowcast model using a Gauss-Markov Kalman filter algorithm in which the background is specified by the IRI. The IRI (Bilitza, 2001) is an empirical model that specifies various ionospheric parameters on a monthly basis, away from the auroral zone and during undisturbed conditions. IRI draws upon observations from various sources including ionosondes, incoherent coherent radar, and spacecraft. The latitude-longitude-altitude resolution of the GIS output is 2.5° by 5° by 20 km. Lin, Lin, Rajesh, et al. (2020) and Wang et al. (2021) employed GIS data to describe the planetary wave response of the ionosphere to Sudden Stratospheric Warmings. The GIS data set has been shown to be useful in resolving the day-to-day tidal variability of the F-region ionosphere (Oberheide, 2022). These studies demonstrate the suitability of the GIS data set for removal of the ionospheric effect on the identification of non-migrating tides in $\Sigma O/N_2$.

2.3. ICON-EUV O^+ Profiles

The ICON Extreme Ultraviolet spectrograph (ICON-EUV) is an imaging spectrometer that derives limb profiles of dayglow in a spectral range from 54 to 88 nm (Sirk et al., 2017). Altitude profiles of O^+ are inferred from the 61.7 nm O^+ triplet and the 83.4 nm O^+ triplet (Stephan et al., 2017). Here, we use Version 3 of the derived O^+ density profiles. ICON-EUV O^+ density profiles have been compared to observations from COSMIC-2, ground-based ionosondes, and incoherent scatter radar from 2019 to 2021. Wautelet et al. (2022) reported that EUV peak density (NmF2) is on the order 50%–60% smaller than each of these datasets and that the differences in peak height HmF2 is consistent with the expected precision of the various data sources. Day-to-day variation in the bias of the EUV parameters are believed to be caused by effects due to ICON's orbital precession, precision of the calibrations, or limitations of the EUV inversion during prolonged and exceptional low solar activity. Nevertheless, ICON-EUV provides the spatial structure of the daytime ionospheric density required to remove global-scale ionospheric effects on the identification of non-migrating tides in $\Sigma O/N_2$. Since, the ICON-FUV disk and ICON-EUV limb sampling of a particular combination of local solar time and location is offset in time, our correction based on ICON-EUV O+ profiles (Section 3) is calculated using 45-day running means. Any mean potential offset in NmF2 is addressed by our methodology (Section 3).

2.4. Simulation of $\Sigma O/N_2$ by the TIEGCM-ICON

In Section 5 we refer to $\Sigma O/N_2$ modeled by the Thermosphere-Ionosphere-Electrodynamics General Circulation Model for the Ionospheric Connection Explorer (TIEGCM-ICON; Maute, 2017). In this version of the TIEGCM, the lower boundary at ∼97 km is perturbed by atmospheric tides derived from the ICON-MIGHTI observations of horizontal winds (Harding et al., 2017) and temperature (Stevens et al., 2018) to simulate the thermospheric and ionospheric conditions in the real-time atmosphere experienced by ICON. The Hough Mode Extension (HME) technique (Cullens et al., 2020; Forbes et al., 2017) is applied to MIGHTI temperature and horizontal winds (∼90–103 km altitude range) to self-consistently specify the global tidal spectrum in neutral winds and temperature throughout the thermosphere. We note that there are some limitations to this approach because of the asymmetrically incomplete latitudinal/longitudinal sampling afforded by ICON-MIGHTI. Since ICON-MIGHTI samples latitudes from 10°S to 40°N and misses a large sector of longitudes in the southern hemisphere due to the SAA, tidal aliasing can lead to higher uncertainties in the tides (Cullens et al., 2020; Forbes et al., 2017). In Section 5, we compare amplitudes derived from a full tidal decomposition of the modeled $\Sigma O/N_2$ to those derived from the ICON-FUV data set. Using TIE-GCM-ICON output, a modeled $\Sigma O/N_2$ can be calculated relative to the standard N_2 column depth of 10^{17} molecule cm^{-2}, first specified by Strickland et al. (1995); also see Meier (2021).

3. Removing Ionospheric Contamination From Column O/N_2 Retrieved by ICON-FUV

Since $\Sigma O/N_2$ is derived from the ratio of the shortwave (SW) channel to the longwave (LW) channel column emission rates, the effects of ionospheric contamination can be reduced in the retrieval of $\Sigma O/N_2$ by subtracting an estimate of the ionospheric contribution from the SW radiance. We estimate the ionospheric contribution by calculating path integrals from the ICON observatory to the disk retrieval location at 150 km, the altitude used to geolocate the disk retrieval. The 135.6 nm emission of ionospheric origin can be modeled (Equation 1) as the sum of contributions from radiative recombination between electrons and oxygen ions (first term) and ion-ion mutual neutralization (second term).

Table 1
Summary of Coefficients Used in Equation 1

α_{1356}	Radiative recombination rate	$7.3 \times 10^{-13} \times (1160/T_e)^{0.5}$
β_{1356}	Ion-ion neutralization yield	0.54
k_1	Radiative attachment	1.3×10^{-15}
k_2	Ion-ion neutralization rate	10^{-7}
k_3	Ion-atom neutralization rate	1.4×10^{-10}

Note. All values are based on the work of Meléndez-Alvira et al. (1999) and references therein.

$$I_{RR} = \frac{1}{10^6}\int \alpha_{1356}(T_e) N_e \left[O^+\right] ds + \frac{\beta_{1356} k_1 k_2}{10^6}\int \frac{N_e [O]\left[O^+\right]}{k_2\left[O^+\right] + k_3 [O]} ds \quad (1)$$

Equation 1 ignores multiple scattering of 135.6 nm photons that is considered in the nighttime ionospheric retrievals (Kamalabadi et al., 2018). Depending on the viewing conditions and solar activity, the multiple scattering effect is of the order of 2%–7% of the SW dayglow (Meier et al., 2015). Equation 1 also ignores the weak source of OI 135.6 nm emission from dissociative excitation of O_2 by energetic photoelectrons that is included in the ICON disk $\Sigma O/N_2$ algorithm of Meier (2021) and data products used in their analysis. The radiative recombination term is the principal term (Meier, 1991). A description of the constants in Equation 1 is provided by Table 1 (Meléndez-Alvira et al., 1999). The line of sight from the spacecraft to the disk retrieval location is discretized into 50 segments for which a value for electron temperature T_e, electron density N_e, and atomic oxygen density [O] is calculated. In Equation 1, we assume that $N_e = \left[O^+\right]$ which is true for the F-region ionosphere where the bulk of the ionospheric emissions originate (Johnson, 1966). NRLMSISE-00 (Picone et al., 2002) and IRI are used to specify [O] and T_e, respectively. As stated earlier, we test three data sets for specification of the electron density term: GIS, the IRI, and the ICON EUV spectrometer. Electron density along the line of sight is determined using GIS and IRI output by using the nearest neighbor model grid point. Figure 2 shows a day's worth of ionospheric contribution estimates based on GIS electron density on 27 March 2020 along the orbit track of the ICON observatory. Cleary visible are the equatorial arcs as afternoon local solar times are sampled in the southern hemisphere and morning local solar times are sampled in the northern hemisphere. For the modified data set based on ICON-EUV, since ICON-EUV limb O^+ retrievals and ICON-FUV $\Sigma O/N_2$ retrievals are not sampled at the same local solar time and location for a given day, a sliding 45-day window climatology is used to determine N_e based on observed O^+ profiles. The average is taken of EUV O^+ limb profiles within the 45-day window whose tangent location is within 15 deg longitude, 0.5 deg latitude and 20 min local solar time of the line of sight location at 300 km. We leave out the following O^+ profiles from the average: (a) those with a reported EUV quality flag greater than 1 which correspond to retrievals not recommended for use in any analysis, (b) those with NmF2 greater than 4.8×10^6 cm^{-3}, and (c) those with NmF2 greater than 3 standard deviations of the mean NmF2 during the 45-day window. The cutoff value of 4.8×10^6 cm^{-3}, following the work of Chang et al. (2013), is based on long-term ionosonde observations by Liu et al. (2006) who found that NmF2 maximized at about 3×10^6 cm^{-3} for F10.7 cm index about equal to 300 sfu.

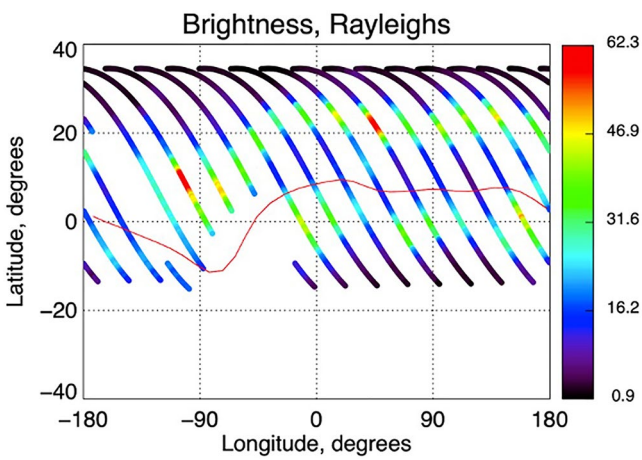

Figure 2. Based on COSMIC-2 Global Ionospheric Specification, the modeled ionospheric contribution (Rayleighs) to the daytime shortwave channel signal from the Ionospheric Connection Explorer FUV imager on 27 March 2020 mapped as a function of longitude and latitude. Plotted in red is the geomagnetic equator.

The analysis presented in the following section uses Level 1 Version 3 ICON-FUV data products (calibrated radiances) which are now known to be too high by about 30% (Frey et al., 2023). To account for this and calibrate our calculations of the ionospheric contribution to the emission at 135.6 nm (Equation 1), we determine a scale factor which is applied to the modeled ionospheric emissions. The scale factor is determined by comparing our model to observed ICON-FUV shortwave limb radiances during nighttime, when the total emission is due to the ionosphere. Three weeks of data are used for each time period. The comparison is limited to data between ±15° magnetic latitude, between 21:00 and 24:00 LST, and at a solar zenith angle greater than 110°. The altitude resolution of the ICON-FUV limb profiles (~4 km) is degraded to match that of GIS output (20 km). The quantity for comparison is the average radiance between 20 and 40 km above the altitude of the peak. To account for the line of sight in this calculation which is now directed at the limb, the path integral (Equation 1) to calculate the column brightness extends past the limb tangent point back up to ICON's orbit altitude.

Figure 3 shows scatter plots comparing the observed ICON-FUV SW brightness against the modeled brightness based on the GIS ionosphere, from DOY 73–94 (Figure 3a) and DOY 265–273 (Figure 3b) in 2020 at the sampling of

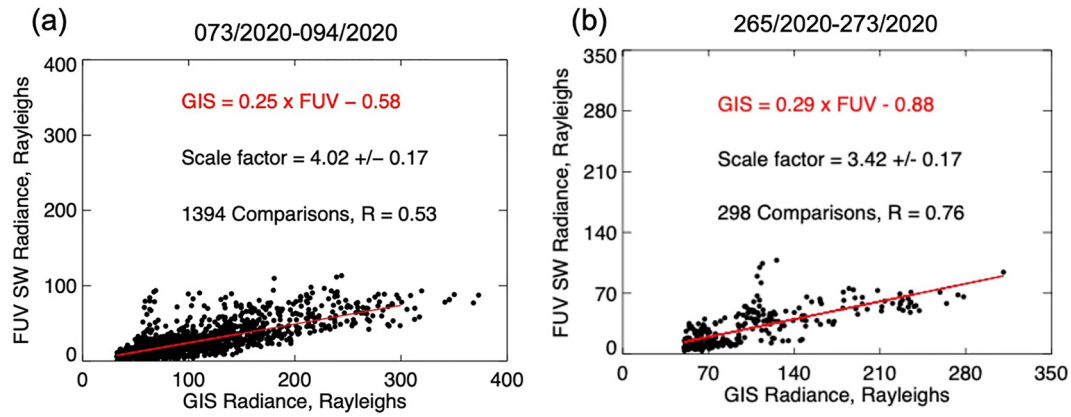

Figure 3. Comparison of observed nighttime radiance at 135.6 nm by the FUV instrument onboard the Ionospheric Connection Explorer to modeled radiance at 135 nm based on electron density maps from GIS. Comparisons are from days 73–94 of 2020 during conditions as specified by the text. Uses Version 3 ICON-FUV L1 data which is the basis of the subsequent results. Printed on the figure are the line of best fit, the GIS-to-FUV scale factor and its uncertainty, the number of comparisons, and the linear correlation coefficient of the observations and model results after the scale factor adjustment. The line of best fit is plotted in red.

magnetic latitude/LST and observing geometry discussed above. The equation for the line of best fit, scale factor (inverse of the slope) and its uncertainty, and linear correlation coefficient (R) are shown in each panel. Our analysis for Version 3 yields a scale factor equal to 4.02 ± 0.17 for DOY 73–94 and 3.42 ± 0.17 for DOY 265–273. The DOY 265–273 period was used as the basis for a scale factor for DOY 218–241 due to a scarcity of data and the sampling during that time period. Increasing our calculated brightness based on GIS by a factor of ∼4 normalizes our model to the relative sensitivity of the ICON-FUV instrument in Version 3 and allows us to properly treat for ionospheric contamination. These scale factors are consistent with the work of Wautelet et al. (2021) who found a mean positive difference of 55% between ICON-FUV and COSMIC-2 values for nighttime NmF2. Note that the ionospheric radiative recombination emission is proportional to the square of the ionospheric density (Equation 1). Figure S1 in Supporting Information S1 file is the same as Figure 3a except that it is based on Version 5 Level 1 ICON-FUV SW radiances in the comparisons. This yields a scale factor of 2.38 ± 0.09 demonstrating that the calibration has improved between Versions 3 and 5. Evidently, the scale factor depends on the accuracy of the calibration for each version. We emphasize that the choice between Version 3 and 5 has no impact on our approach or the key results of this work. The scale factor used to normalize the modeled ionospheric contribution based on IRI is assumed to be equal to that determined for GIS since IRI serves as the background to the GIS data assimilation scheme. This ensures that GIS and IRI are equally calibrated to the ICON-FUV instrument sensitivity with the main difference in the datasets being that GIS can resolve the longitudinal-local solar time variations introduced by non-migrating tides.

ICON-EUV does not retrieve O^+ profiles at night, therefore a direct comparison to ICON-FUV as was done for GIS is not possible. However, the calculated values (Equation 1) based on ICON-EUV can be compared to those based on GIS. Consequently, we determine a scale factor to apply to the calculated value based on EUV to normalize to those based on GIS. The scale factor to apply to ICON-EUV to normalize to ICON-FUV is then the product of two scale factors. The EUV-to-GIS scale factor is determined by comparing the magnitude of the respective brightness intensities along the ICON-FUV $\Sigma O/N_2$ retrieval. Ordered pairs are formed consisting of GIS and EUV brightness intensities in increasing order in terms of magnitude. The scale factor is derived from the line of best fit of these ordered pairs. This approach is necessary, since the calculated GIS- and EUV-based brightness are uncorrelated and would not yield a linear trend in a point-to-point comparison. For the 73–94 time period, the GIS-EUV scale factor was determined to be ∼6. Therefore, the EUV-FUV scale factor is ∼24. Likewise, the scale factor for the 218–241 period was determined to be ∼6.7. Figure S2 in Supporting Information S1 file presents the GIS-EUV comparisons as well as the line of best fit and uncertainty in the scale factors. The necessity to scale EUV in this manner is consistent with the findings of Wautelet et al. (2022) who found that EUV is on average 56% smaller than coincident values from COSMIC-2. Based on the biases reported by Wautelet et al. (2021, 2022), a scale factor ∼16–24 is not out of the realm of reasonability.

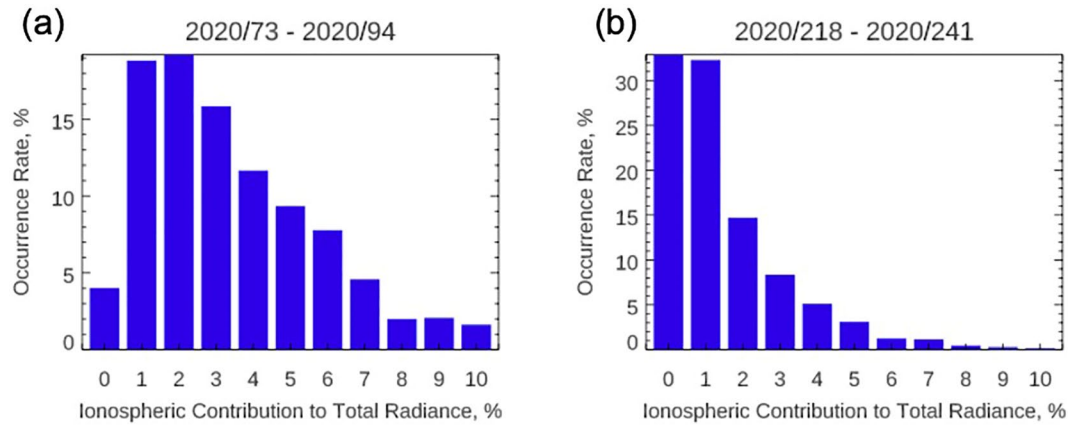

Figure 4. The distribution of ionospheric contribution to the total radiance at 135.6 nm observed by ICON-FUV during (a) days 73–94 and (b) days 218–241 in 2020 based on the GIS data set. Data are located between 17.5° and 22.5° latitude on the descending node of the ICON orbit.

The next step in reprocessing the FUV disk data is to run the operational ICON-FUV $\Sigma O/N_2$ algorithm with modified SW radiances from which the ionosphere contribution has been subtracted. This is done for each the three models of the ionospheric contribution: GIS, IRI, and EUV. Uncertainties in the ionospheric contributions are estimated using the standard deviation of the five closest points. To propagate the uncertainty in the ionospheric contribution into the retrieval of $\Sigma O/N_2$, these uncertainties are added in quadrature with the uncertainty in the unmodified SW radiances. On average, this addition increases the uncertainty in the SW radiances by about 3%–7%.

To identify non-migrating tides, we perform longitudinal wavenumber decomposition as a function of latitude and day (local time) during different seasons: March–April 2020 and August–September 2020. The decomposition was carried out for the original and modified datasets in order to quantify the effects of the ionospheric contamination. Data for each day are averaged into 5° latitude bins. Following a similar approach to that of He et al. (2010), at each latitude, data are fitted to a zonal mean and Fourier modes corresponding to wavenumbers 1–4 using Equation 2 where λ is longitude in radians and $A_0, A_1, \ldots A_8$ are the fitting coefficients.

$$A_0 + A_1\cos\left(\frac{\lambda}{2\pi}\right) + A_2\sin\left(\frac{\lambda}{2\pi}\right) + A_3\cos\left(2\frac{\lambda}{2\pi}\right) + A_4\sin\left(2\frac{\lambda}{2\pi}\right) + A_5\cos\left(3\frac{\lambda}{2\pi}\right) + A_6\sin\left(3\frac{\lambda}{2\pi}\right) + A_7\cos\left(4\frac{\lambda}{2\pi}\right) + A_8\sin\left(4\frac{\lambda}{2\pi}\right) \quad (2)$$

The respective amplitude and phase for wavenumber n are given by $\sqrt{A_n^2 + A_{n+1}^2}$ and $\tan^{-1}\frac{A_{n+1}}{A_n}$. To determine the fitting coefficients and their uncertainties, we perform a least squares fit in which measure errors are specified by the reported uncertainties in the retrieved values for $\Sigma O/N_2$. Uncertainty in the derived amplitudes and phases are determined by propagating the uncertainties in the fitting coefficients. In Section 4 we discuss differences in the longitudinal wave structure seen between the original and GIS-, IRI-, and EUV-based modified datasets during the two time periods.

4. Results

Figure 4 presents histograms showing the occurrence rate of the ionospheric contribution to the total shortwave (SW) radiance during the two time periods examined: DOY 73–94 (Figure 4a) and DOY 218–241 (Figure 4b), both in 2020, and hereafter referred to as time period 1 and time period 2. These plots were produced using the modified data set based on GIS electron density. Similar plots for the modified datasets based on either IRI or ICON-EUV exhibit similar trends and are thus not shown here but are in Supporting Information S1 file (Figures S3 and S4). The data sampled for these histograms are at 20° latitude on the descending node of the ICON orbit (to match the data set used in the analysis corresponding to Figure 5 that follows). Neighboring latitude bins track well with the behavior of the 20° latitude bin in the results that follow. The distribution is presented as the

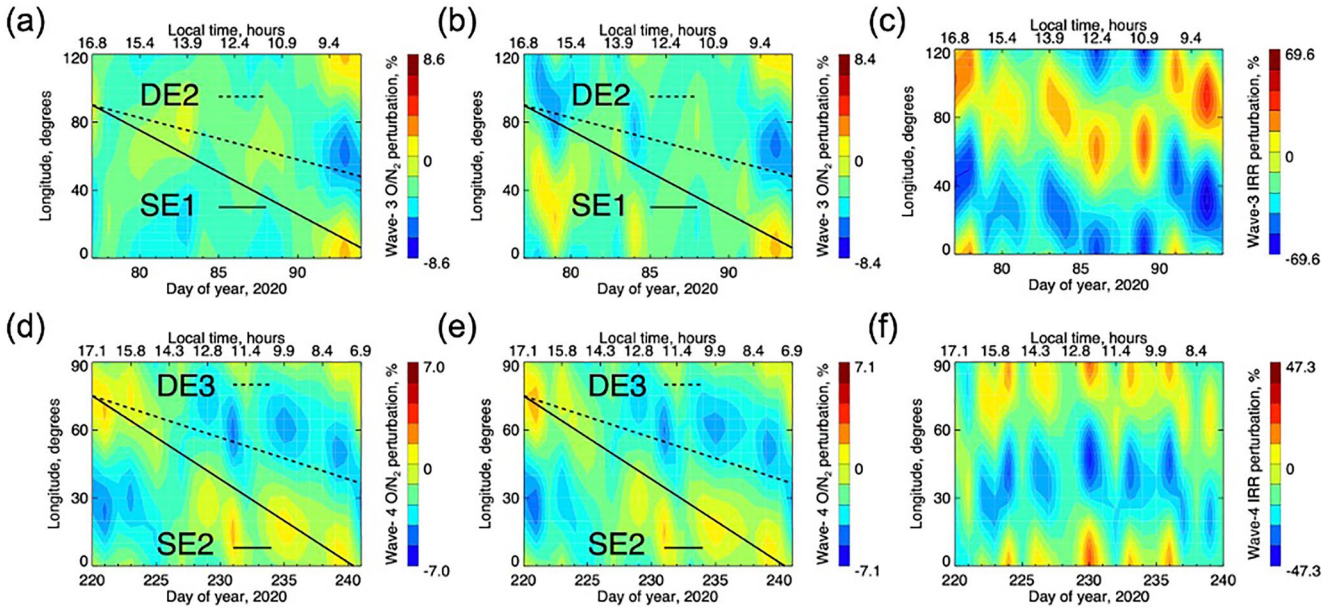

Figure 5. (a) Longitudinal wavenumber-3 reconstruction as a function of longitude and day of year (local time) in the original $\Sigma O/N_2$ data set during a time period in March-April 2020 at 20°N on the descending node portion of the ICON orbit. Presented as percent deviation about the background zonal mean $\Sigma O/N_2$. The DE2 and SE1 phase slopes are shown for reference as dashed and solid lines respectively. (b) Same as (a) but for the modified $\Sigma O/N_2$ data set based on GIS data. (c) Longitudinal wavenumber-3 reconstruction of the GIS-based estimated ionospheric contribution to the SW radiances used in the $\Sigma O/N_2$ retrieval. Units of percent relative to the zonal mean SW radiance. Panels (d–f) are the same as (a–c) except for a time period in August–September 2020 and the DE3 and SE2 phase slopes are shown for reference.

occurrence rate (percent of all data points satisfying the above sampling criteria) of ionospheric contribution as a percent of the total SW radiance. On average, the DOY 73–94 time period has a higher ionospheric contribution (4.2%) than that during the DOY 218–241 time period (2%). About 5% of retrievals during time period 2 have ionospheric contribution greater than 5%, while more than 25% of retrievals during time period 1 have ionospheric contribution greater than 5%. About 65% of retrievals during time period 2 have ionospheric contribution less than 2%, compared to less than 25% of retrievals during time period 1. It is noteworthy that this bias is also present in both the estimates based on IRI and ICON-EUV (Figures S3 and S4 in Supporting Information S1). This has implications on the expected differences seen between the original data set and the modified data set; the reduction of the ionospheric contamination in the $\Sigma O/N_2$ retrieval should affect the signature of non-migrating tides more during time period 1 than during time period 2.

Solar and geomagnetic activity levels were explored as possible reasons for the difference between time periods 1 and 2. It was found that the respective F10.7 and Ap indices were similar during each time period. The mean F10.7 during time period 1 was only 4% higher than that during time period 2. The median Ap indices were respectively 5 and 4 during time periods 1 and 2. Therefore, differences in solar or geomagnetic activity variation do not explain why the ionospheric contribution to SW is higher during time period 1 than that during time period 2. Note also that the mean unmodified total SW radiance during time periods 1 and 2 were within 1% of each other. The root cause of the difference in the modeled ionospheric contribution during the two periods is the higher average electron density present in GIS during time period 1 as compared to that during time period 2. The mean daytime GIS NmF2 between 15°N and 25°N was about 18% higher during time period 1 than that during time period 2. Since the dominant term of Equation 1 depends on the square of the electron density, it is not surprising that the modeled ionospheric contribution is about a factor of 2 greater during time period 1 than that during time period 2. Additionally, the mean nighttime GIS NmF2 between 15°N and 25°N during the two time periods agree within a percent. Thus, the bias between the time periods does not translate to the scale factor used to adjust the modeled ionospheric radiances.

Kil et al. (2013) found that in GUVI data during 2002 August 31–September 2, the ionospheric contribution can be as large 10% around the equatorial ionization anomaly around 15:00 LT. Figure 4b indicates negligible occurrence rate for ionospheric contribution larger than 7% during 2020 at a similar time of year to the analysis

of Kil et al. (2013). Although, it is worthwhile to note that 2002 experienced much higher solar activity than in 2020. Higher solar activity should produce a higher percentage of the ionospheric contribution to the total signal at 135 nm because (a) total electron content (TEC) increases by about a factor of 5 from solar minimum to maximum (Lean et al., 2011), and (b) the total dayglow at 135.6 nm increases by about a factor of 3 from solar minimum to maximum (Meier et al., 2015).

Figure 5 provides a summary of the longitudinal–local time variation of $\Sigma O/N_2$ and the estimated ionospheric contribution to the SW radiance decomposed into a wavenumber-3 pattern during time period 1 and a wavenumber-4 pattern during time period 2. Data used during each time period were between 17.5° and 22.5° latitude on the descending node of the ICON orbit. There were low solar and geomagnetic conditions during both time periods. Each panel in Figure 5 shows the longitudinal wavenumber reconstruction as a function of longitude and day of year. As indicated by the upper horizontal axis, the orbital coverage of local solar time is a function of day of year, decreasing with the precession of the ICON orbit. These plots are generated based on the amplitudes and phases computed by fitting for Fourier coefficients using Equation 2 as discussed in the previous section. The amplitudes and phases and their uncertainties are presented in Supporting Information S1 file (refer to Figures S5, S6, S7, and S8). The error bars therein reflect the propagation of the uncertainties in the Fourier coefficients (Equation 2) used to calculate amplitude and phase. Large amplitude/phase variations can be interpreted as the result of a combination of day-to-day variability, the presence of multiple tides, and random uncertainty (~5%–10%; England et al., 2021) in the retrieved values of $\Sigma O/N_2$. Figures 5a and 5b respectively show the wave-3 pattern during time period 1 in the original data set and the modified data set based on GIS. Figures 5d and 5e are the same as Figures 5a and 5b except for the wave-4 pattern in $\Sigma O/N_2$ during time period 2. Figures 5c and 5f respectively show the wave-3 and wave-4 pattern in the ionospheric contribution during time period 1 and time period 2.

It is evident that the wave-3 pattern changes after 12:00 LST in the original data set during time period 1 (Figure 5a). For reference, the theoretical phase slopes of DE2 (120° longitude/24 hr) and SE1 (120° longitude/12 hr) are shown respectively as dashed and solid lines. The morphology in Figure 5a clearly does not match either slope. After correction for the ionospheric contamination, the wave-3 pattern in the GIS-modified data set obviously tracks the phase slope of DE2 (Figure 5b). The ionospheric contribution to the SW radiance during the afternoon hours of Figure 5a has a strong eastward propagation seen in the wave-3 decomposition of Figure 5c, which masks the true tidal signal. The eastward propagation of the ionospheric contribution likely reflects the E-region dynamo modulation by DE2 tidal winds which leads to the variations aloft in the F-region ionosphere (Immel et al., 2006; Sagawa et al., 2005).

In contrast to period 1, during time period 2 there is negligible difference in wave-4 between the original data set (Figure 5d) and the GIS-modified data set (Figure 5e). The DE3 and SE2 theoretical phase slopes are shown to indicate to the reader that the local time progression resembles that expected for SE2 rather than DE3. Figure 5f indicates an approximately stationary pattern in the wave-4 decomposition of the ionospheric contribution to 135.6 nm during the afternoon hours. This stationary pattern seems to vanish at the beginning of time period 2. The cause of this difference between the two time periods can be best explained by Figure 4 which shows that on average the ionospheric contribution to the total SW radiance is lower during time period 2 than during time period 1. The correction for ionospheric contamination during time period 2 (Figure 5d) is sufficiently small that there is little change in the pattern (Figure 5e).

5. Discussion of Results

In order to provide insight and understanding of the tidal signatures observed in Section 4, we introduce model expectations using TIEGCM-ICON and Hough Mode Extensions (Section 2.4). Figure 6 shows tidal amplitudes in $\Sigma O/N_2$ calculated from TIEGCM-ICON during time period 1 and time period 2 at 20° latitude. For time periods 1 and 2, wavenumber-3 and wavenumber-4 tides are shown respectively. The total wavenumber-3 perturbation caused by tides is a superposition of DE2 and SE1, along with a more minor contribution from DW4 and SW5. DE2 is the strongest or equal strongest wave-3 tide throughout the time period. Similarly, the total wavenumber-4 perturbation caused by tides is a superposition of DE3 and DW5, along with a more minor contribution from SE2 and SW6. DE3 is the dominant wave-4 tide during time period 2 except at the very beginning when DW5 is largest. The modeled amplitudes seem to underestimate the total wavenumber-3 and wavenumber-4 amplitudes from the ICON analysis in Figure 5 but do match the dominant tide apparent in the observations. This tendency

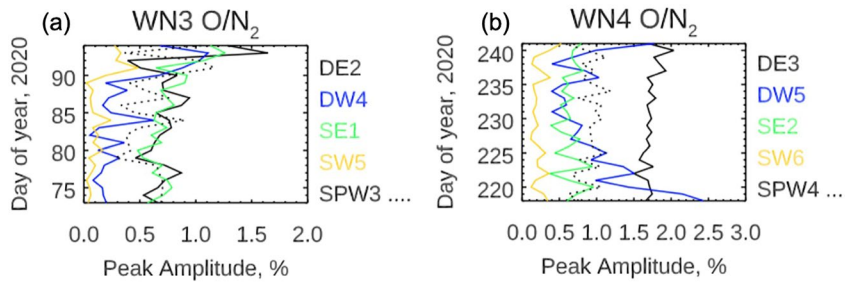

Figure 6. (a) Wavenumber-3 tidal amplitudes around 20° latitude as a function of day of year modeled by TIEGCM-ICON during a time period in March-April 2020. (b) Same as (a) except for wavenumber-4 during a time period in August–September 2020.

to underestimate the tidal amplitude in $\Sigma O/N_2$ is consistent with the earlier findings of England et al. (2021), who did not correct the ICON SW data for radiative recombination.

Figure 7 summarizes the relevant tides from HME-ICON output. These HME tides reflect only tides propagating from the lower atmosphere and do not include any that may be generated above ~105 km altitude. Tides for which ICON-HME specification is not available are not shown in Figure 7, that is, DW4, SW5, DW5, SW6. Peak amplitudes (as a function of altitude) at 20° latitude in temperature and zonal/meridional winds are shown as a

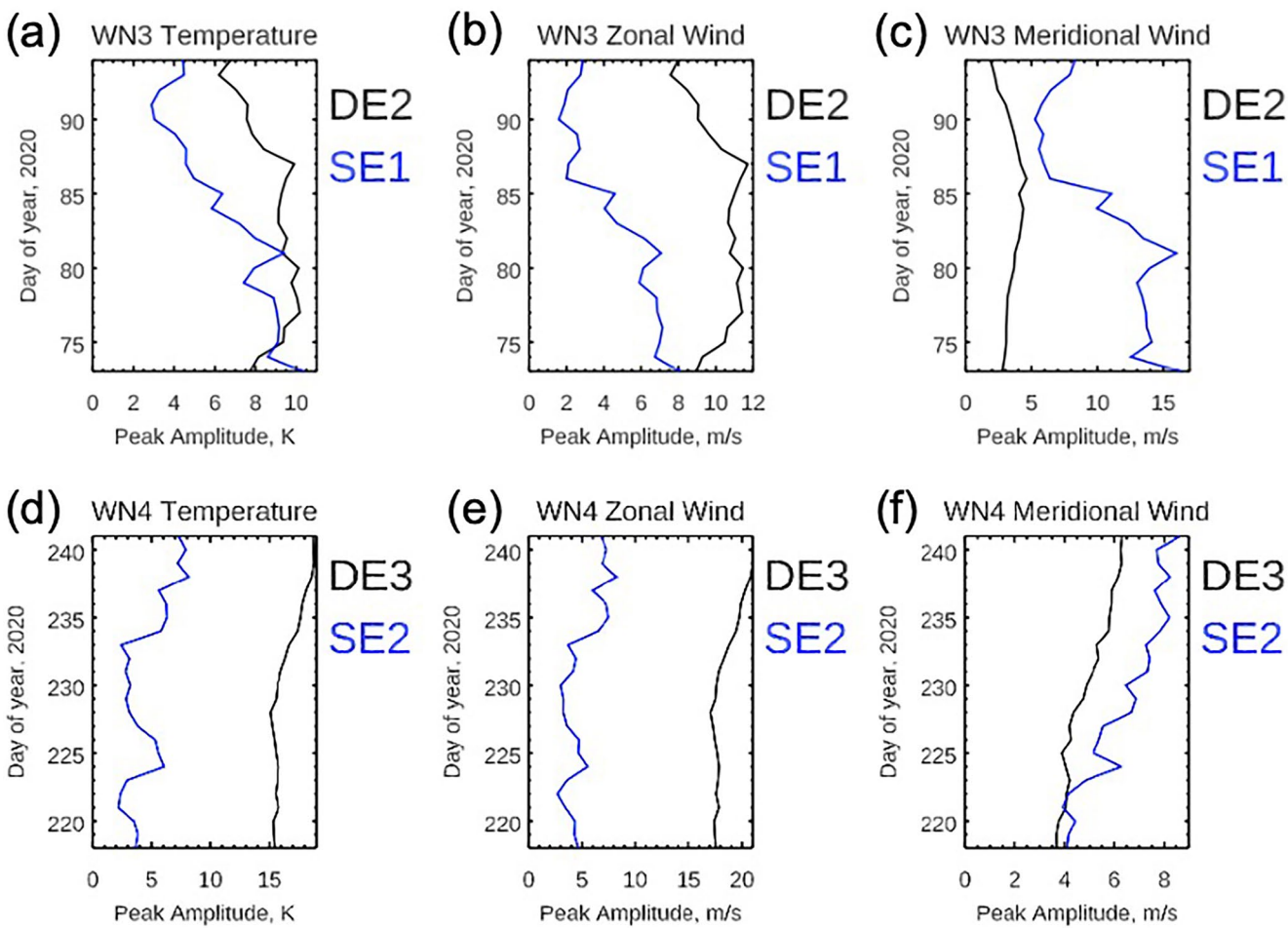

Figure 7. ICON Hough Mode Extension wavenumber-3 tide peak amplitudes around 20° latitude as a function of day of year in temperature (a), zonal wind (b) and meridional wind (c) during DOY 73–94. The respective wavenumber-4 amplitudes during DOY 218–241 are shown in (d–f).

function of day during each time period. DE2 (DE3) are the strongest wavenumber-3 (4) tides in temperature and zonal wind throughout their respective time period which is consistent with their long vertical wavelengths. The presence of DE2 in the modified $\Sigma O/N_2$ (Figure 5b) data set is consistent with both the HME output and the fact that DE2 has an exceptionally long vertical wavelength (the vertical wavelength of DE2's first symmetric mode is 108 km; Truskowski et al., 2014) allowing DE2 to be prominent in the vertically integrated $\Sigma O/N_2$. This suggests that the GIS-modified $\Sigma O/N_2$ data set faithfully reflects the tidal dynamics in thermospheric composition during time period 1. The eastward trend seen in Figures 5d and 5e is consistent with the expectation that DE3 is the strongest wavenumber-4 tide (with SE2 also playing role) and this is confirmed by HME output during time period 2. The phase slope reflects SE2, which indicates that the wavenumber-4 origin is more complex than solely being caused by DE3. This is consistent with the conclusion of a case study of wavenumber-4 tides that employed physics-based empirical modeling and observations from the TIMED and CHAMP satellites (Oberheide et al., 2011). Note that the vertical wavelength of the most important Hough mode to SE2 is much longer than that for DE3, making it not so surprising that SE2 can be more prominent in $\Sigma O/N_2$. The vertical wavelength of SE2's most important Hough mode (first antisymmetric) is 183 km while that of DE3's (first symmetric mode) is 56 km (Truskowski et al., 2014).

It is worthwhile to compare this work to previous findings based on TIMED/GUVI data. Kil et al. (2013) estimated the ionospheric contamination of $\Sigma O/N_2$ to be 5%–10% from 31 August to 2 September 2002, much larger than the typical values seen in Figure 5. Kil et al. (2013) proved that the longitudinal variation at a fixed local time were caused by ionospheric contamination of GUVI data during that time period. In contrast, the results in the previous section show that at least some of the time, the ionospheric contribution does not modulate the longitudinal variation in ICON-FUV data. The solar activity was much higher in 2002 than in 2020 which may partially explain the difference in results as the ionospheric contribution is expected to be greater at higher solar activity (see discussion in Section 4). On the other hand, Zhang et al. (2010) found that wave-3 and wave-4 peak to valley vary from 7% to 11% in TIMED/GUVI data in 2009, a period of very low solar activity. Such amplitudes are in better agreement with ICON-FUV (Figures S5 and S7 in Supporting Information S1 file) and thus also higher than the TIEGCM-ICON amplitudes. Given how few estimates of tides in $\Sigma O/N_2$ exist, it is not fully known why TIEGCM-ICON underestimates the observed amplitudes. England et al. (2021) compared the tidal signature in $\Sigma O/N_2$ with TIE-GCM and hypothesized that discrepancy in the tidal vertical wavelength in the model could be the cause. The tides may vary over the 35-day averaging widow used to derive the Hough Mode Extensions which force the lower boundary of the TIEGCM-ICON. Dedicated mechanistic model studies and regular observations of tides in $\Sigma O/N_2$, made possible by the approach presented in this paper, are required to resolve the discrepancy.

6. Conclusions

Isolating and quantifying purely thermospheric tidal perturbations in $\Sigma O/N_2$ leads to a more complete description of tidal-ionosphere coupling. In this paper, we have presented a method that removes most of the ionospheric contamination of the retrieval of $\Sigma O/N_2$ from measurements by the FUV imager onboard the Ionospheric Connection Explorer. In doing so, we have presented the first investigation of the tidal longitudinal—local time evolution of $\Sigma O/N_2$ that is not compromised by ionospheric contamination effects. We assessed estimates of the ionospheric contribution based on either the GIS, IRI, or ICON-EUV datasets which are adjusted, based on the biases between the ionospheric specifications and the airglow. After removing the ionospheric signal from the SW data, we reran the ICON-FUV operational disk retrieval algorithm to provide corrected $\Sigma O/N_2$. In turn, we reexamine the longitudinal wavenumber-3 and wavenumber-4 structure during times from March to April 2020 and August and September 2020, respectively, noting differences between the original and modified $\Sigma O/N_2$ datasets. This work presents a framework for application to $\Sigma O/N_2$ datasets from other science missions and motivates further modeling/theoretical analyses. A list of conclusions from this study is as follows:

1. Scale factors for increasing the GIS/IRI/EUV based calculations of the ionospheric contribution to daytime 135.6 nm were calculated to properly reduce the ionospheric contamination in Version 3 ICON-FUV SW radiances. This accounts for differences between the various versions of the ICON-FUV Level 1 radiances. Such analyses should be performed on a version-by-version basis for each specification of electron density.
2. In the modified $\Sigma O/N_2$ data set based on GIS ionospheric corrections, a DE2-like pattern is evident in the longitudinal wavenumber-3 variations during March–April 2020. HME-ICON tides and TIEGCM-ICON

confirm that DE2 is present during that time. Ionospheric contamination of the original data set masked the DE2-like pattern. This suggests that the GIS-based correction closely reflects the real atmosphere.

3. Observed amplitudes are higher than those modeled by TIEGCM-ICON in agreement with the earlier study by England et al. (2021).
4. No difference in the longitudinal wavenumber-4 structure is observed between the original and modified $\Sigma O/N_2$ during August–September 2020 because the ionospheric correction is much lower than in the earlier period. In contrast, Kil et al. (2013) showed that the ionospheric contamination dominated the retrieved tidal response seen in GUVI $\Sigma O/N_2$ during the same season in 2002. The most probable cause for this inconsistency is the much higher solar activity in 2002 than that in 2020. Future work will reproduce this analysis on ICON data collected during the anticipated solar maximum.
5. There is greater ionospheric contribution to the SW radiance during March-April 2020 than during August–September 2020, which causes the more pronounced change in the modified $\Sigma O/N_2$ in the former time period.

Data Availability Statement

All ICON data are available at ftp://icon-science.ssl.berkeley.edu/pub/ and the NASA Space Physics Data Facility (https://spdf.gsfc.nasa.gov). GIS data are made available by National Cheng Kung University at http://formosat7.earth.ncku.edu.tw/ (registration required). The modified O/N_2 datasets used in this work are preserved at the Virginia Tech Data Repository (https://doi.org/10.7294/21538380).

Acknowledgments
ICON is supported by NASA's Explorers Program through contracts NNG12FA45C and NNG12FA42I. This work was supported by NASA contract 80GSFC18C0061 and NSF award 2149697. RRM received partial support from the Civil Service Retirement System.

References

Bilitza, D. (2001). International reference ionosphere 2000. *Radio Science*, *36*(2), 261–275. https://doi.org/10.1029/2000rs002432

Chang, L. C., Lin, C.-H., Yue, J., Liu, J.-Y., & Lin, J.-T. (2013). Stationary planetary wave and nonmigrating tidal signatures in ionospheric wave 3 and wave 4 variations in 2007–2011 FORMOSAT-3/COSMIC observations. *Journal of Geophysical Research: Space Physics*, *118*(10), 6651–6665. https://doi.org/10.1002/jgra.50583

Christensen, A. B., Paxton, L. J., Avery, S., Craven, J., Crowley, G., Humm, D. C., et al. (2003). Initial observations with the Global Ultraviolet Imager (GUVI) in the NASA TIMED satellite mission. *Journal of Geophysical Research*, *108*(A12), 1451. https://doi.org/10.1029/2003JA009918

Correira, J., Evans, J. S., Lumpe, J. D., Krywonos, A., Daniell, R., Veibell, V., et al. (2021). Thermospheric composition and solar EUV flux from the Global-scale Observations of the Limb and Disk (GOLD) mission. *Journal of Geophysical Research: Space Physics*, *126*(12), e2021JA029517. https://doi.org/10.1029/2021JA029517

Cui, J., Yelle, R. V., Li, T., Snowden, D. S., & Müller-Wodarg, I. C. F. (2014). Density waves in Titan's upper atmosphere. *Journal of Geophysical Research: Space Physics*, *119*(1), 490–518. https://doi.org/10.1002/2013JA019113

Cullens, C. Y., Immel, T. J., Triplett, C. C., Wu, Y.-J., England, S. L., Forbes, J. M., & Liu, G. (2020). Sensitivity study for ICON tidal analysis. *Progress in Earth and Planetary Science*, *7*(1), 18. https://doi.org/10.1186/s40645-020-00330-6

England, S. L. (2012). A review of the effects of non-migrating atmospheric tides on the Earth's low-latitude ionosphere. *Space Science Reviews*, *168*(1–4), 211–236. https://doi.org/10.1007/s112140119842-4

England, S. L., Immel, T. J., Huba, D., Hagan, M. E., Maute, A., & DeMajistre, R. (2010). Modeling of multiple effects of atmospheric tides on the ionosphere: An examination of possible coupling mechanisms responsible for the longitudinal structure of the equatorial ionosphere. *Journal of Geophysical Research*, *115*(A5), A05308. https://doi.org/10.1029/2009JA014894

England, S. L., Meier, R. R., Frey, H. U., Mende, S. B., Stephan, A. W., Krier, C. S., et al. (2021). First results from the retrieved column O/N_2 ratio from the Ionospheric Connection Explorer (ICON): Evidence of the impacts of nonmigrating tides. *Journal of Geophysical Research: Space Physics*, *126*(9), e2021JA029575. https://doi.org/10.1029/2021JA029575

Evans, J. S., Strickland, D. J., Huffman, R. E., & Eastes, R. W. (1995). Satellite remote sensing of thermospheric O/N_2 and solar EUV, 2. Data analysis. *Journal of Geophysical Research*, *100*(A7), 12217–12226. https://doi.org/10.1029/95JA00573

Forbes, J. M., Russell, J., Miyahara, S., Zhang, X., Palo, S., Mlynczak, M., et al. (2006). Troposphere-thermosphere tidal coupling as measured by the SABER instrument on TIMED during July–September 2002. *Journal of Geophysical Research*, *111*(A10), A10S06. https://doi.org/10.1029/2005JA011492

Forbes, J. M., Zhang, X., Hagan, M. E., England, S. L., Liu, G., & Gasperini, F. (2017). On the specification of upward-propagating tides for ICON science investigations. *Space Science Reviews*, *212*(1–2), 697–713. https://doi.org/10.1007/s11214-017-0401-5

Forbes, J. M., Zhang, X., Palo, S., Russell, J., Mertens, C. J., & Mlynczak, M. (2008). Tidal variability in the ionospheric dynamo region. *Journal of Geophysical Research*, *113*(A2), A02310. https://doi.org/10.1029/2007JA012737

Frey, H., Mende, S. B., Meier, R. R., Kamaci, U., Urco, J. M., Kamalabadi, F., et al. (2023). In flight performance of the Far Ultraviolet Instrument (FUV) on ICON. *Space Science Reviews*, *219*, 23. https://doi.org/10.1007/s11214-023-00969-9

Goncharenko, L. P., Chau, J. L., Liu, H.-L., & Coster, A. J. (2010). Unexpected connections between the stratosphere and ionosphere. *Geophysical Research Letters*, *37*(10), L10101. https://doi.org/10.1029/2010GL043125

Hagan, M. E., & Forbes, J. M. (2002). Migrating and nonmigrating diurnal tides in the middle and upper atmosphere excited by tropospheric latent heat release. *Journal of Geophysical Research*, *107*(D24), 4754. https://doi.org/10.1029/2001JD001236

Harding, B. J., Makela, J. J., Englert, C. R., Marr, K. D., Harlander, J. M., England, S. L., & Immel, T. J. (2017). The MIGHTI wind retrieval algorithm: Description and verification. *Space Science Reviews*, *212*(1–2), 585–600. https://doi.org/10.1007/s11214-017-0359-3

He, M., Liu, L., Wan, W., Lei, J., & Zhao, B. (2010). Longitudinal modulation of the O/N_2 column density retrieved from TIMED/GUVI measurement. *Geophysical Research Letters*, *37*(20), L20108. https://doi.org/10.1029/2010GL045105

Immel, T. J., England, S. L., Mende, S. B., Heelis, R. A., Englert, C. R., Edelstein, J., et al. (2018). The ionospheric connection explorer mission: Mission goals and design. *Space Science Reviews*, *214*(1), 13. https://doi.org/10.1007/s11214-017-0449-2

Immel, T. J., Sagawa, E., England, S. L., Henderson, S. B., Hagan, M. E., Mende, S. B., et al. (2006). Control of equatorial ionospheric morphology by atmospheric tides. *Geophysical Research Letters*, *33*(15), L15108. https://doi.org/10.1029/2006GL026161

Johnson, C. Y. (1966). Ionospheric composition and density from 90 to 1200 kilometers at solar minimum. *Journal of Geophysical Research*, *71*(1), 330–332. https://doi.org/10.1029/JZ071i001p00330

Jones, M., Jr., Forbes, J. M., & Hagan, M. E. (2014). Tidal-induced net transport effects on the oxygen distribution in the thermosphere. *Geophysical Research Letters*, *41*(14), 5272–5279. https://doi.org/10.1002/2014GL060698

Kamalabadi, F., Qin, J., Harding, B. J., Iliou, D., Makela, J. J., Meier, R. R., et al. (2018). Inferring nighttime ionospheric parameters with the far ultraviolet imager onboard the ionospheric connection explorer. *Space Science Reviews*, *214*(4), 70. https://doi.org/10.1007/s11214-018-0502-9

Kil, H., Lee, W. K., Shim, J., Paxton, L. J., & Zhang, Y. (2013). The effect of the 135.6 nm emission originated from the ionosphere on the TIMED/GUVI O/N_2 ratio. *Journal of Geophysical Research: Space Physics*, *118*(2), 859–865. https://doi.org/10.1029/2012JA018112

Kil, H., & Paxton, L. J. (2011). The origin of the nonmigrating tidal structure in the column number density ratio of atomic oxygen to molecular nitrogen. *Geophysical Research Letters*, *38*(19), L19108. https://doi.org/10.1029/2011GL049432

Krier, C. S., England, S. L., Greer, K. R., Evans, J. S., Burns, A. G., & Eastes, R. W. (2021). Deducing non-migrating diurnal tides in the middle thermosphere with GOLD observations of the Earth's far ultraviolet dayglow from geostationary orbit. *Journal of Geophysical Research: Space Physics*, *126*(10), e2021JA029563. https://doi.org/10.1029/2021JA029563

Lean, J. L., Meier, R. R., Picone, J. M., & Emmert, J. T. (2011). Ionospheric total electron content: Global and hemispheric climatology. *Journal of Geophysical Research*, *116*(A10), A10318. https://doi.org/10.1029/2011JA016567

Lee, W. K., Kil, H., Paxton, L. J., Zhang, Y., & Shim, J. S. (2013). The effect of geomagnetic-storm-induced enhancements to ionospheric emissions on the interpretation of the TIMED/GUVI O/N_2 ratio. *Journal of Geophysical Research: Space Physics*, *118*(12), 7834–7840. https://doi.org/10.1002/2013JA019132

Lieberman, R. S., Oberheide, J., & Talaat, E. R. (2013). Nonmigrating diurnal tides observed in global thermospheric winds. *Journal of Geophysical Research: Space Physics*, *118*(11), 7384–7397. https://doi.org/10.1002/2013JA018975

Lin, C. Y., Lin, C. C., Liu, J., Rajesh, P. K., Matsuo, T., Chou, M., et al. (2020). The early results and validation of FORMOSAT-7/COSMIC-2 space weather products: Global Ionospheric specification and Ne-Aided Abel electron density profile. *Journal of Geophysical Research: Space Physics*, *125*(10), 1–12. https://doi.org/10.1029/2020JA028028

Lin, C. Y., Matsuo, T., Liu, J. Y., Lin, C. H., Huba, J. D., Tsai, H. F., & Chen, C. Y. (2017). Data assimilation of ground-based GPS and radio occultation total electron content for global ionospheric specification. *Journal of Geophysical Research: Space Physics*, *122*(10), 10876–10886. https://doi.org/10.1002/2017JA024185

Lin, J. T., Lin, C. H., Rajesh, P. K., Yue, J., Lin, C. Y., & Matsuo, T. (2020). Local-time and vertical characteristics of quasi-6-day oscillation in the ionosphere during the 2019 Antarctic Sudden stratospheric warming. *Geophysical Research Letters*, *47*(21). https://doi.org/10.1029/2020GL090345

Liu, L., Wan, W., Ning, B., Pirog, O. M., & Kurkin, V. I. (2006). Solar activity variations of the ionospheric peak electron density. *Journal of Geophysical Research*, *111*(A8), A08304. https://doi.org/10.1029/2006JA011598

Maute, A. (2017). Thermosphere-ionosphere-electrodynamics general circulation model for the ionospheric connection explorer: TIEGCM-ICON. *Space Science Reviews*, *212*(1–2), 523–551. https://doi.org/10.1007/s11214-017-0330-3

Meier, R. R., Picone, J. M., Drob, D., Bishop, J., Emmert, J. T., Lean, J. L., et al. (2015). Remote sensing of Earth's limb by TIMED/GUVI: Retrieval of thermospheric composition and temperature. *Earth and Space Science*, *2*, 1–37. https://doi.org/10.1002/2014EA000035

Meier, R. R. (1991). Ultraviolet spectroscopy and remote sensing of the upper atmosphere. *Space Science Reviews*, *58*, 1–186. https://doi.org/10.1007/BF01206000

Meier, R. R. (2021). The thermospheric column O/N_2 ratio. *Journal of Geophysical Research: Space Physics*, *126*(3), e2020JA029059. https://doi.org/10.1029/2020JA029059

Meléndez-Alvira, D. J., Meier, R. R., Picone, J. M., Feldman, P. D., & McLaughlin, B. M. (1999). Analysis of the oxygen nightglow measured by the Hopkins Ultraviolet Telescope: Implications for ionospheric partial radiative recombination rate coefficients. *Journal of Geophysical Research*, *104*(A7), 14901–14914. https://doi.org/10.1029/1999JA900136

Mende, S. B., Frey, H. U., Rider, K., Chou, C., Harris, S. E., Siegmund, O. H. W., et al. (2017). The far ultra-violet imager on the ICON mission. *Space Science Reviews*, *212*(1–2), 655–696. https://doi.org/10.1007/s11214-017-0386-0

Oberheide, J. (2022). Day-to-day variability of the semidiurnal tide in the F-region ionosphere during the January 2021 SSW from COSMIC-2 and ICON. *Geophysical Research Letters*, *49*(17), e2022GL100369. https://doi.org/10.1029/2022GL100369

Oberheide, J., Forbes, J. M., Zhang, X., & Bruinsma, S. L. (2011). Wave-driven variability in the ionosphere- thermosphere-mesosphere system from TIMED observations: What contributes to the "wave 4". *Journal of Geophysical Research*, *116*(A1), A01306. https://doi.org/10.1029/2010JA015911

Oberheide, J., Mlynczak, M. G., Mosso, C. N., Schroeder, B. M., Funke, B., & Maute, A. (2013). Impact of tropospheric tides on the nitric oxide 5.3 μm infrared cooling of the low-latitude thermosphere during solar minimum conditions. *Journal of Geophysical Research: Space Physics*, *118*(11), 7283–7293. https://doi.org/10.1002/2013JA019278

Pedatella, N. M., Forbes, J. M., Maute, A., Richmond, A. D., Fang, T.-W., Larson, K. M., & Millward, G. (2011). Longitudinal variations in the F region ionosphere and the topside ionosphere-plasmasphere: Observations and model simulations. *Journal of Geophysical Research*, *116*(A12), A12309. https://doi.org/10.1029/2011JA016600

Picone, J. M., Hedin, A. E., Drob, D. P., & Aikin, A. C. (2002). NRLMSISE-00 empirical model of the atmosphere: Statistical comparisons and scientific issues. *Journal of Geophysical Research*, *107*(A12), SIA15–SIA16. https://doi.org/10.1029/2002JA009430

Roble, R. G., & Shepherd, G. G. (1997). An analysis of wind imaging interferometer observations of O(^{1}S) equatorial emission rates using the thermosphere-ionosphere-mesosphere-electrodynamics general circulation model. *Journal of Geophysical Research*, *102*(A2), 2467–2474. https://doi.org/10.1029/96JA02930

Sagawa, E., Immel, T. J., Frey, H. U., & Mende, S. B. (2005). Longitudinal structure of the equatorial anomaly in the nighttime ionosphere observed by IMAGE/FUV. *Journal of Geophysical Research*, *110*(A11), 11302. https://doi.org/10.1029/2004JA010848

Sirk, M. M., Korpela, E. J., Ishikawa, Y., Edelstein, J., Wishnow, E. H., Smith, C., et al. (2017). Design and performance of the ICON EUV spectrograph. *Space Science Reviews*, *212*(1–2), 631–643. https://doi.org/10.1007/s11214-017-0384-2

Stephan, A. W., Korpela, E. J., Sirk, M. M., England, S. L., & Immel, T. J. (2017). Daytime ionosphere retrieval algorithm for the Ionospheric Connection Explorer (ICON). *Space Science Reviews*, *212*(1–2), 645–654. https://doi.org/10.1007/s11214-017-0385-1

Stephan, A. W., Meier, R. R., England, S. L., Mende, S. B., Frey, H. U., & Immel, T. J. (2018). Daytime O/N_2 retrieval algorithm for the ionospheric connection explorer (ICON). *Space Science Reviews*, *214*(1), 42. https://doi.org/10.1007/s11214-018-0477-6

Stevens, M. H., Englert, C. R., Harlander, J. M., England, S. L., Marr, K. D., Brown, C. M., & Immel, T. J. (2018). Retrieval of lower thermospheric temperatures from O_2 A band emission: The MIGHTI experiment on ICON. *Space Science Reviews*, *214*(1), 4. https://doi.org/10.1007/s11214-017-0434-9

Strickland, D. J., Evans, J. S., & Paxton, L. J. (1995). Satellite remote sensing of thermospheric O/N_2 and solar EUV, 1. Theory. *Journal of Geophysical Research*, *100*(12), 217. https://doi.org/10.1029/95JA00574

Truskowski, A. O., Forbes, J. M., Zhang, X., & Palo, S. E. (2014). New perspectives on thermosphere tides - 1. Lower thermosphere spectra and seasonal-latitudinal structures. *Earth Planets and Space*, *66*, 136. https://doi.org/10.1186/s40623-014-0136-4

Wang, J. C., Palo, S. E., Forbes, J. M., Marino, J., Moffat-Griffin, T., & Mitchell, N. J. (2021). Unusual quasi 10-day planetary wave activity and the ionospheric response during the 2019 Southern Hemisphere sudden stratospheric warming. *Journal of Geophysical Research: Space Physics*, *126*(6), e2021JA029286. https://doi.org/10.1029/2021JA029286

Wautelet, G., Hubert, B., Gérard, J.-C., Immel, T. J., Frey, H. U., Mende, S. B., et al. (2021). First ICON-FUV nighttime NmF2 and hmF2 comparison to ground and space-based measurements. *Journal of Geophysical Research: Space Physics*, *126*(11), e2021JA029360. https://doi.org/10.1029/2021JA029360

Wautelet, G., Hubert, B., Gérard, J. C., Immel, T. J., Sirk, M. M., Korpela, E. J., et al. (2022). Comparison of ICON-EUV F-peak characteristic parameters with external data sources. *Space Science Reviews*, *218*(8), 62. https://doi.org/10.1007/s11214-022-00930-2

Zhang, Y., England, S., & Paxton, L. J. (2010). Thermospheric composition variations due to nonmigrating tides and their effect on ionosphere. *Geophysical Research Letters*, *37*(17), L17103. https://doi.org/10.1029/2010GL044313

Zhang, Y., Paxton, L. J., & Schaefer, R. (2021). Ionospheric and thermospheric contributions in TIMED/GUVI O 135.6 nm radiances. *Journal of Geophysical Research: Space Physics*, *126*(9), e2021JA029333. https://doi.org/10.1029/2021JA029333